Estimating damage parameters of a CuCrZr alloy subjected to two varying heat treatments using small punch test

V.D. Vijayanand [a,b,*], M. Mokhtarishirazabad [b], Y. Wang [c], M. Gorley [c], D.M. Knowles [b], M. Mostafavi [b]

[a] Metallurgy and Materials Group, Indira Gandhi Centre for Atomic Research, Kalpakkam 603102, India
[b] Department of Mechanical Engineering, University of Bristol, Bristol BS8 1TR, UK
[c] United Kingdom Atomic Energy Authority, Culham Science Centre, Abingdon OX14 3DB, UK

ABSTRACT

Small punch testing was carried out on Copper-Chromium-Zirconium alloy subjected to two heat treatment conditions –both quenched and one subjected to subsequent aging. The variation in the load-displacement characteristics associated with the testing was attributed to differences in plastic and damage properties evolved as a consequence of these two varying heat treatments. The influence of these properties varied in different regimes of the load-displacement curve. In this work the elastic and plastic properties derived from uniaxial tensile tests performed on materials subjected to these two heat treatment conditions were used to simulate the initial stages of the load-displacement curve. Using an inverse finite element method, the parameters relevant to a Gurson-Tvergaard-Needleman based damage model which influence the later stages of the load-displacement curve were estimated. The variations in the damage model's parameters with respect to heat treatment conditions were correlated with fractographic observations. A formulation for compliance correction of small punch testing rig using finite element model incorporating elastic and plastic properties has also been discussed.

© 2021 Elsevier B.V. All rights reserved.

1. Introduction

Copper-Chromium-Zirconium (CuCrZr) alloy is proposed to be used as a heat sink material in the EU-DEMO reactor. Its superior thermal conductivity and strength makes it a primary choice for divertor components [1–7]. This material derives its strength predominantly from chromium rich precipitates which form during aging [2,4,6]. The microstructure of this alloy is sensitive to heat treatment parameters, careful control of which would result in best combination of strength, ductility and stability during neutron irradiation [5,6,8].

In this work, the deformation behavior of CuCrZr is investigated after subjecting it to two heat treated conditions –water quenched and aged using small punch testing (SPT) technique. SPT is one of the rapidly emerging miniature specimen test techniques [9–11]. Correlating small punch data to data obtained from conventional uniaxial test systems is crucial for its applicability on a wider scale. Several empirical formulations have been proposed for cross-correlating to uniaxial test data, many of which are material dependent and are specific to respective experimental set-up [9,11–13]. The use of inverse finite element method based approach is an alternative for empirical correlations but can be computationally intensive [14–19]. The paramount factor which limits development of reliable correlation with respect to uniaxial test data is the associated complex state of stress which evolves during testing [11,20,21]. For a small punch test carried out at a constant deformation rate, the elastic and plastic properties of the material dominate only in the initial stages of deformation [17,22]. It is the damage which evolves due to the complex state of stress, which dictates the load-displacement characteristics during the later stages of loading. The inherent tri-axial state of stress generated during small punch testing makes it an alternative to notched specimen testing for studying damage evolution in materials.

The Gurson-Tvergaard-Needleman (GTN) model has been traditionally used to simulate damage evolution caused by microvoids [23,24]. GTN model quantifies the dilatational deformation process using micro-mechanical parameters which establish criteria for failure. This is applicable to ductile materials where microvoid nucleation and growth occurs leading to additional instability in the material. The use of GTN model has helped in simulating the entire load-displacement curve of SPT [18,22,25,26].

* Corresponding author at: Metallurgy and Materials Group, Indira Gandhi Centre for Atomic Research, Kalpakkam 603102, India.
E-mail addresses: vdvijayanand@igcar.gov.in, vd.vijayanand@gmail.com (V.D. Vijayanand).

In this work the initial stages of the SPT's load-displacement characteristics of CuCrZr in both quenched and aged conditions were simulated using experimentally obtained plastic properties. The later stages of the curve were simulated using GTN model whose micro-mechanical parameters were estimated using an inverse finite element method. The variations in GTN parameters with respect to the two heat treated conditions are then correlated with the fractographic observations.

2. Material, experimental and simulation methods

The chemical composition of the CuCrZr alloy used in the current investigation was Cu-1Cr-0.1Zr (all in wt.%). Swab etching was done using a solution comprising of 5 g ferric chloride, 20 ml hydrochloric acid and 100 ml ethanol for microstructural investigation. Grain size measurement was done using Heyn intercept method. Both tensile specimens and SPT specimens were machined from rods of 16 mm diameter and 100 mm length. All the specimens were subjected to solution heat treatment at a temperature of 1000 °C for 30 min in a molten salt bath and then water quenched. For producing the aged specimens an additional heat treatment was given in a vacuum furnace at 475 °C for 2 h. The tensile specimen had a gauge diameter of 5.65 mm and a gauge length of 27 mm. Uniaxial testing was carried out at ambient room temperature using an electro-mechanical system equipped with a load cell whose capacity was 100 kN at a nominal strain rate of $1 \times 10^{-3} s^{-1}$. The displacement was acquired using a video extensometer which comprised of a camera with a resolution of 2.4 megapixels. The maximum acquisition frame rate was 50.8 Hz. The procedure for tensile testing was compliant with ASTM E8M-21 standard. The small punch specimen had a diameter of 8 mm and thickness of 500 ± 5 μm. The receiving hole in the lower die had a diameter of 4 mm and the diameter of the punch tip was 2.5 mm. The design and dimensions of the SPT rig was compliant with the CEN standard [27]. The SPT rig was attached to a servo-hydraulic machine and a cross head velocity of 0.005 mms^{-1} was employed during loading which was done at ambient room temperature. The load cell attached to the system was operated in the range of ± 5 kN. The inverse finite element analysis simulation was carried out by coupling Matlab R2018a with Abaqus CAE 6.14-1.

3. Results

3.1. Uniaxial tensile properties

The optical micrographs of CuCrZr alloy in quenched and aged condition are shown in Fig. 1. The average grain size in both the conditions was 45 μm. The engineering stress-strain data for both
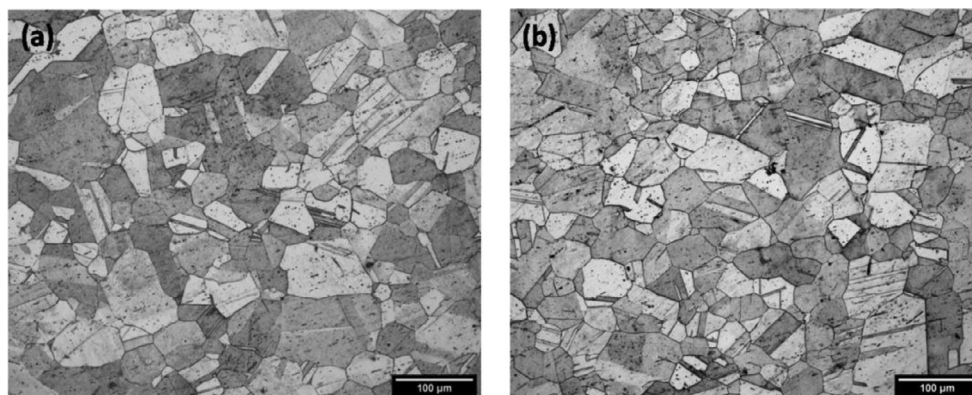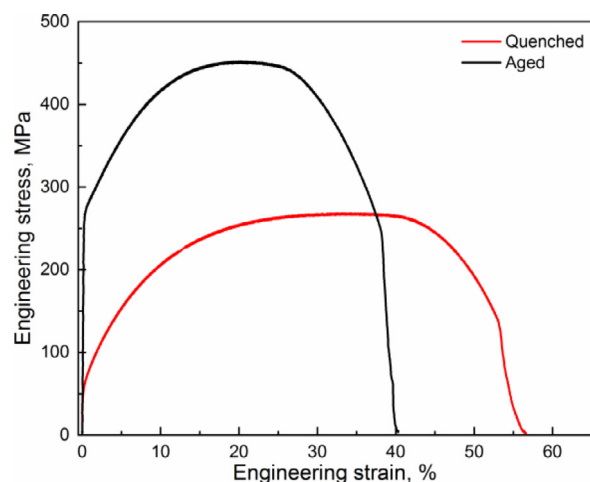

Fig. 2. Engineering stress-strain curves of CuCrZr in quenched and aged conditions.

Table 1
Tensile properties of CuCrZr in quenched and aged conditions.

	Quenched	Aged
0.2% offset yield stress, MPa	58	272
Ultimate tensile strength, MPa	267	452
Elongation, %	57	40
Reduction in area, %	82	73

quenched and aged conditions are shown in Fig. 2. The properties obtained from the tensile tests are given in Table 1. The elongation and area reduction of the quenched sample was much higher than what was observed in the aged condition.

3.2. Compliance correction for SPT test rig

As only the displacement of the punch was monitored in the current investigation, appropriate corrections had to be made to account for the testing rig's compliance. The compliance is dependent on the SPT rig and its determination is essential for estimating the actual specimen deformation [28]. Use of empirical formulations is the most common practice to convert cross-head displacement to the specimen deformation [29]. These formulations assume a uniform proportional deviation between the punch and the specimen displacements in all the deformation regimes. However, compliance of the set-up is likely to influence the load-displacements characteristics in the regime were elastic deformation is dominant.

Fig. 1. Microstructure of CuCrZr in (a) quenched and (b) aged conditions.

In this work a new FEM based method has been proposed to estimate the compliance of the test set-up. For this an Abaqus based two-dimensional axisymmetric FE model was generated whose geometry was identical to the actual experimental set-up. The punch, lower and upper dies were assumed as rigid bodies. The deformable element type used for the specimen was a 4-node bi-linear axisymmetric quadrilateral (CAX4R). A uniform mesh size of 0.03 mm was used. The Young's modulus of 123 GPa [30] and Poisson's ratio of 0.3 were used to populate the elastic properties. The plastic properties were obtained from the uni-axial tensile testing the results of which have been discussed in the previous section. A quasi-static loading was assumed in this analysis. Separate formulations for compliance correction were derived for the quenched and aged conditions. A displacement controlled loading was used in the simulation and the models pertaining to both quenched and aged conditions were deformed up to punch displacement of 2.5 mm.

The displacement values for the simulated curve were taken from both the upper and lower surface nodes along the specimen axis (Fig. 3a). Fig. 3(b) and (c) show the comparison between the experimental and simulated load-displacement curves for the quenched and aged conditions. The experimental displacement values in these figures pertain to the punch displacement. The experimental displacement was higher than both the simulated displacements due to the compliance associated with SPT rig. The deviation in experimental displacement and the simulated displacement taken from the upper surface node (USN) increased proportion-

ately and became constant in both the quenched and aged specimens. However, the deviation between the experimental displacement and the displacement from the lower surface node (LSN) increased proportionately up to failure. This is because the LSN displacement takes into account the thickness reduction of the specimen being tested. As the displacement from the USN does not consider this 'specimen-thinning' effect, this was taken as reference to calculate the compliance of the system.

The progressive increase in deviation between the experimental displacement and USN's displacement in the initial stages of deformation indicates that the compliance of the system is dominant only up to a certain threshold load. An alternate approach wherein both proportional and offset corrections can be incorporated for compliance correction would generate a representative load-displacement curves suitable for further analysis. In this approach, estimating the critical load (L_c) at which the proportional deviation changes to offset deviation is crucial. For its determination the experimental displacement values were offset in step sizes of -0.005 mm until most of the data in both these curves superimposed. The offset was optimized in such a way that the average difference between the simulated and experimental displacement values in the 'superimposed regime' was in the range of $\pm$0.005 mm as shown in (Fig. 4 (a) and (b)). The load at which the superimposed regime commenced was recorded as L_c. The superimposed regime approximately corresponds to the plastic and the membrane stretching deformation stages. A clear demarcation of the deformation stages in the load-displacement curve is presented sub-
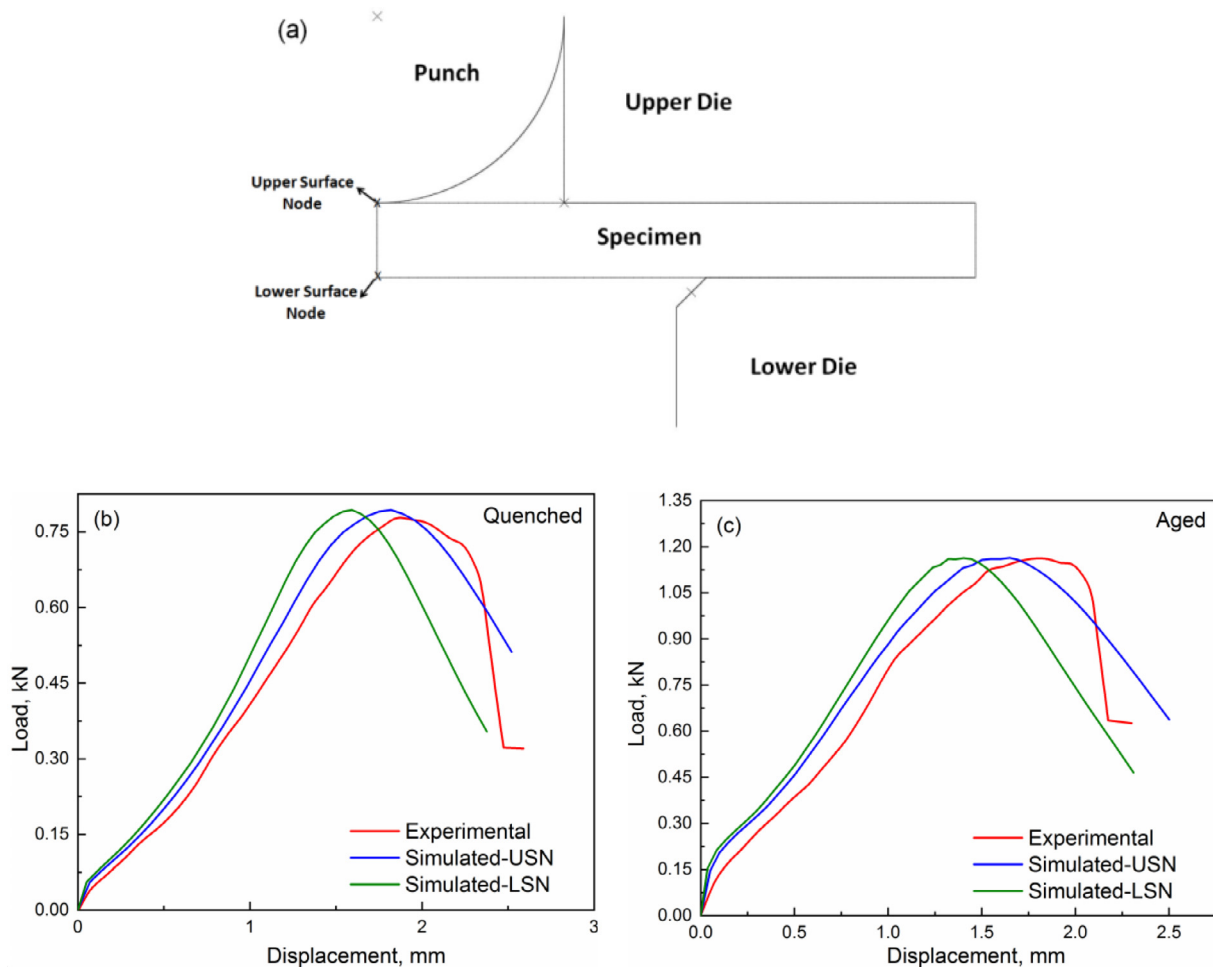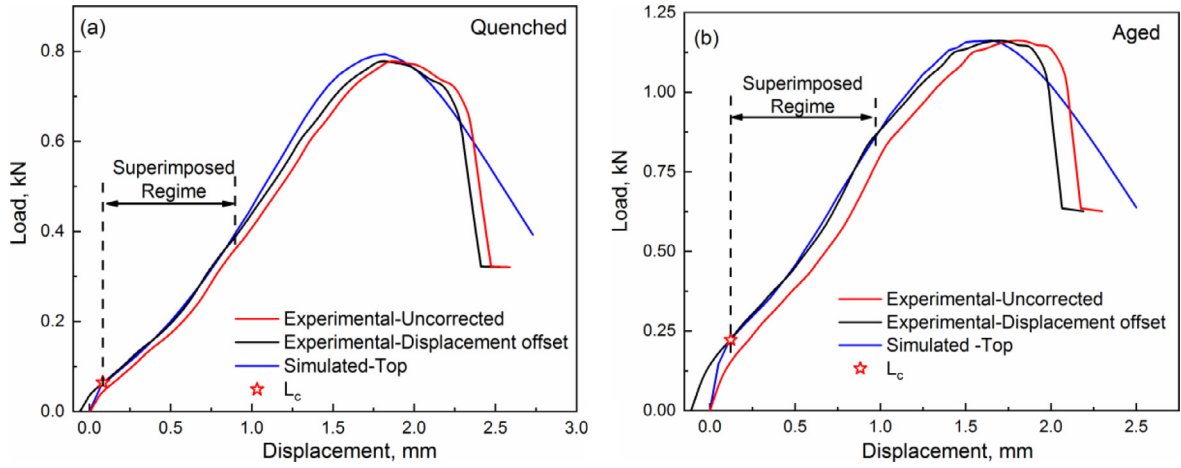

Fig. 3. Location of the (a) upper surface node (USN) and lower surface node (LSN) in the finite element model. Comparison of the experimental and simulated load-displacement curves in (b) quenched and (c) aged conditions.

Fig. 4. Plot of experimental, optimised offset experimental and simulated load-displacement data from the upper surface node (USN) for the (a) quenched and (b) aged conditions. The location of the critical load L_c is also indicated in the respective plots.

sequently. As the model used in the compliance correction scheme only incorporated the elastic and plastic properties it had limitation in simulating the later stages of the load-displacement curve.

The proportional factor (PF) and the offset factor (OF) were determined by using the following expression.

$$PF = \frac{L_c}{(D_{expc} - D_{simc})} \qquad (1)$$

Where D_{expc} and D_{simc} are the experimental and simulated displacements at the critical load L_c

$$OF = D_{expc} - D_{simc} \qquad (2)$$

The corrected displacements D_{cor} were obtained from the experimental displacements D_{exp} using the following correlation

$$D_{cor} = \begin{cases} D_{exp} - \frac{L}{PF} \; if \; L \leq L_c \\ D_{exp} - OF \; if \; L > L_c \end{cases} \qquad (3)$$

Where L is the load corresponding to the experimental displacement D_{exp}.

The critical load (L_c) was 0.0646 and 0.222 for the quenched and aged conditions respectively. The location of L_c and the corrected experimental data are also incorporated in Figs. 4 (a) and (b). The PF for the load-displacement curves of the quenched and aged conditions were 1.25 and 2.06 respectively and those of the OF were 0.0494 and 0.107 respectively. The variations in correction factors of both the heat treatment conditions suggest that in addition to the geometry of the test setup, the microstructure of the material should also be considered for compliance corrections.

3.3. Corrected load-displacement graphs

The corrected graphs along with the various stages of deformation modes are shown in Fig. 5. The peak load in the aged condition was higher (1.25 kN) than that of the quenched condition (0.78 N). The overall displacement at failure was higher (2.24 mm) in the quenched condition, when compared to the aged condition (2.01 mm). The changes in the curvature in the load-displacement curve indicate change in deformation mode. The load-displacement curve comprises of 6 stages each indicating a distinct deformation mode [17,22,31,32]. The first stage (Stage I) is the elastic bending regime after which plastic bending occurs (Stage II). The membrane stretching regime (Stage III) commences after this followed by plastic instability regime (Stage IV). The next stage is the fracture softening regime (Stage V) during which unstable yielding occurs. This is followed by the final stage (Stage VI) when the punch
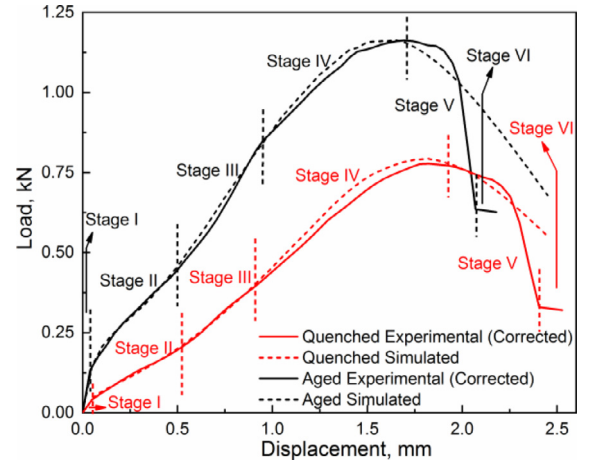
Fig. 5. Plot of corrected and simulated load-displacement curves of both quenched and aged conditions. The various stages of deformation are indicated for both the conditions.

penetrates into the already cracked specimen [33]. The deformation in the initial stages is predominantly dependent on the elastic and plastic properties of the material after which the damage characteristics of the material have a significant influence. The use of only elastic and plastic properties obtained from the uniaxial tensile testing would help to simulate only the first three stages of the small punch curve with reasonable accuracy (Fig. 5). The later stages can be simulated only by incorporating the damage characteristics of the material [34]. In this work a combination of both elastic-plastic properties and GTN damage model was used to simulate the small punch curve up to Stage *V*.

The failure criteria in the GTN model is given by the following expression

$$\Phi(\sigma_{eq}, \sigma_h, \sigma_y, f^*) = \left(\frac{\sigma_{eq}}{\sigma_y(\bar{\varepsilon}_m^p)}\right)^2 + 2q_1 f^* cosh\left(-q_2 \frac{3\sigma_h}{2\sigma_y(\bar{\varepsilon}_m^p)}\right)$$
$$- \left(1 + q_3 f^{*2}\right) = 0 \qquad (4)$$

Where σ_{eq} is the macroscopic von-Mises equivalent, σ_h is the hydrostatic stress, σ_y is the yield stress as a function of $\bar{\varepsilon}_m^p$, the equivalent plastic strain, f^* is the effective void volume fraction, q_1, q_2 and q_3 are calibration parameters.

The effective void volume fraction can be expressed as

$$f^* = \begin{cases} f & \text{if } f \leq f_c \\ f_c + \frac{\overline{f_F} - f_c}{f_F - f_c}(f - f_c) & \text{if } f_c < f < f_F \\ \overline{f_F} & \text{if } f \geq f_F \end{cases} \tag{5}$$

$$\overline{f_F} = \frac{q_1 + \sqrt{q_1^2 - q_3}}{q_3} \tag{6}$$

Where f_c is the critical value for void coalescence, f_F is the void volume fraction at failure.

The rate of total void volume fraction evolution is given by

$$\dot{f} = \dot{f}_{gr} + \dot{f}_{nu} \tag{7}$$

Where $\dot{f}_{gr}$ and $\dot{f}_{nu}$ are rate of growth and nucleation of void volume fraction

$$\dot{f}_{gr} = (1 - f)\dot{\varepsilon}_{kk}^p \tag{8}$$

Where $\dot{\varepsilon}_{kk}^p$ is the plastic strain rate tensor

$$\dot{f}_{nu} = A\dot{\varepsilon}_m^{pl} \tag{9}$$

Where $\dot{\varepsilon}_m^{pl}$ is the equivalent plastic strain rate and

$$A = \frac{f_n}{S_n\sqrt{2\pi}}\exp\left(-\frac{1}{2}\cdot\left(\frac{\bar{\varepsilon}^p - \varepsilon_n}{S_n}\right)^2\right) \tag{10}$$

Where $\bar{\varepsilon}^p$ is the equivalent plastic strain, ε_n is mean strain, and S_n is the standard deviation and f_n is the volume fraction of particles available for void nucleation.
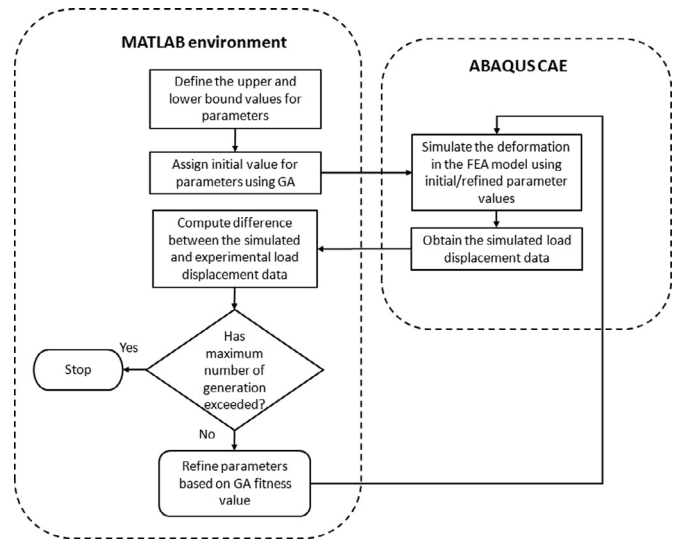
3.4. Inverse finite element model

The GTN based micro-mechanical parameters for both quenched and aged conditions were optimised based on the experimental data. The parameters which were optimised are $f_n, \varepsilon_n, S_n, f_c$ and f_F. In addition to these parameters the co-efficient friction between the specimen and the punch f_{fri} was also optimised. The values of the parameters q_1, q_2 and q_3 which are almost constant for metallic materials were set to 1.5, 1 and 2.25 for both the conditions [18,22,35]. Initial state in both the conditions was assumed to be without any voids.

In this work optimization was carried out using an inverse finite element analysis framework using a genetic algorithm (GA) based Matlab code. GA is a versatile tool for solving optimization problems whose parameters can be adjusted for estimating a near global minimum [36]. The scheme of the procedure is depicted in Fig. 6. The parameters and the bounds which were used for optimization is given in Table 2 and the parameters used for the GA are given in Table 3. The assignment of initial values for the parameters is done by the GA algorithm which generates a random set of 'population' for the first generation. Subsequent refinement of these parameters (either by mutation or crossover) is done based on the difference between the experimental and the simulated data. The closeness between the simulated and experimental data is ranked based on the GA based fitness value. Certain values of parameters in subsequent populations are unaltered (Elite) as they have better fitness values.

Fig. 6. Scheme of inverse finite element method using genetic algorithm (GA) based optimisation tool.

The geometry and element type used in the Abaqus model was similar to what was used for the model which incorporated only the elastic and plastic properties. However, a dynamic-explicit solver was used in this analysis. A biased mesh size ranging from 0.01 mm in the axis to 0.2 mm in the periphery was used in the specimen. Displacement controlled loading was used in these simulations also. The punch displacement in case of quenched specimen was 2.4 mm and for the aged specimen was 2.1 mm. These displacements corresponded to the end of Stage *V* in the respective experimental load-displacement graphs (Fig. 5).

The variation between experimental and simulated values (chi square) and fitness values with generations for both the quenched and aged conditions are given in Fig. 7. The reduction in value of the chi square saturated after initial few generations in both the conditions. The simulated load-displacement graphs with optimized values of the GTN parameters and friction coefficient are shown in Fig. 8 (a and b). The optimized values of the GTN parameters are given in Table 4. There was a marginal variation in the volume fraction of potential nucleating particles, its mean and standard deviation with respect to heat treatment condition. However, the critical volume fraction of voids for coalescence to commence was lower in case of the aged condition. The void volume fraction at failure was much higher in case of the aged condition. The optimized values for friction coefficient were almost the same

Table 3
GA parameters.

Population Size	400
Generations	10
Elite count	50
Crossover count	320
Mutation count	30
Initial population selection mode	Random
Fitness scaling	Rank based
Selection function	Stochastic uniform

Table 4
Optimised values of GTN parameters and friction coefficient for quenched and aged conditions.

	f_n	ε_n	S_n	f_c	f_F	f_{fri}
Quenched	0.050	0.13	0.24	0.033	0.61	0.181
Aged	0.048	0.11	0.23	0.028	0.71	0.185

Table 2
Upper and lower bounds for GA.

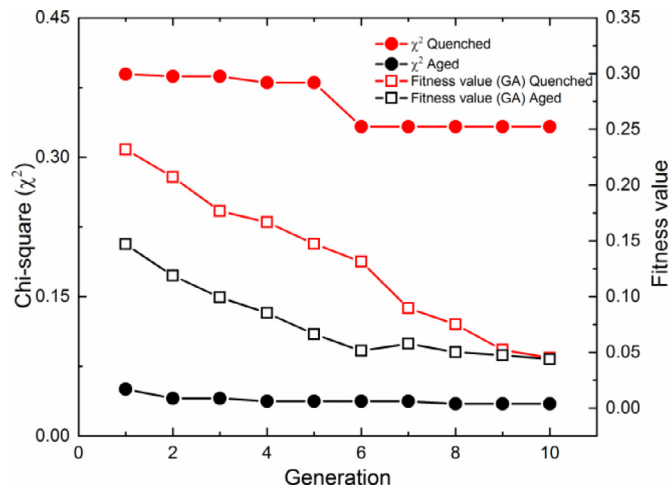|	f_n	ε_n	S_n	f_c	f_F	f_{fri}
Lower Bound	0.001	0.1	0.05	0.009	0.09	0.05
Upper Bound	0.08	0.6	0.35	0.04	0.8	0.25

Fig. 7. Variation of chi-square and fitness value with generation for quenched and aged conditions.

for both the conditions. It has been shown that the friction coefficient is dependent only on the material and test conditions [37]. The current observations establish that the microstructural variations caused by altering heat treatment do not influence this parameter significantly.

3.5. Fractography

Fractographic examination of the failed specimens showed presence of dimples in both the microstructural conditions albeit its relative density was higher in case of the aged condition (Fig. 9). The quenched sample showed a drastic reduction of cross sectional area when compared to the aged condition. The dimples in the fractograph correspond to coalesced voids [38]. The higher void volume fraction in the aged condition can be directly correlated to the presence of more dimples in its fractograph. Though the fraction of the voids at the onset of coalescence was higher in case of the quenched condition, the interlinking of these voids was not prevalent.

Fig. 10 shows the final void volume fraction (VVF) simulated using finite element analysis. The distribution of voids were more localised in case of the aged condition when compared to what was observed in the quenched condition. The reduction in thickness was more prominent in the quenched condition which can be well correlated with the fractographic observations.

The fractographs of the uniaxially tested quenched and aged specimens are shown in Fig. 11 (a and b). As observed in SPT tested specimens, the dimples were fewer in the quenched condition when compared to the aged condition. However, dimple size for the quenched specimen tested under uniaxial testing condition was much larger when compared to those observed for the SPT tested quenched specimen. Since the stress state in the uniaxial and SPT test conditions are quite different, the corresponding fractographic observations cannot be correlated directly. For the uniaxially tested specimen, void nucleation and growth is likely to be significant only beyond necking after which the state of stress changes from uniaxial to tri-axial [39]. In case of the SPT test, the tri-axial state of stress evolves in the membrane stretching regime (Stage III) itself [21].

4. Discussion

Micro-void linked damage in ductile materials comprises of three stages which are nucleation, and growth and interlinking of voids [24,40]. The values of GTN parameters, f_n, f_c and f_F quantify the voids in the nucleating, coalescing and final failure stages respectively. Nucleation of voids generally occurs at interface between second phase particles and the matrix [40,41]. However, in case of single phase systems the voids can nucleate at grain boundaries, twin intersections and dislocation boundaries [42]. Even though the precipitation is less likely to be widespread in the quenched condition, it had a comparable number of void nucleating sites with respect to the aged condition. This can be attributed to presence of other nucleating sites like twin intersections and dislocation boundaries which are generated due to plastic deformation. Though the volume fraction of particles available for void nucleation was almost same for both the microstructural conditions, it required relatively higher plastic strain for the quenched microstructure to activate these nucleating sites.

The critical void fraction at which coalescence occurred was relatively higher in the quenched condition. This suggests that the void nucleation and growth has been significant in this condition before void coalescence. Though the potential sites for void nucleation was comparable in both the heat treated conditions, its growth would be more substantial in the quenched condition as the matrix in is relatively soft. In case of the aged condition, lower void volume fraction for coalescence suggests that the growth of the voids has been suppressed as the matrix was age hardened.
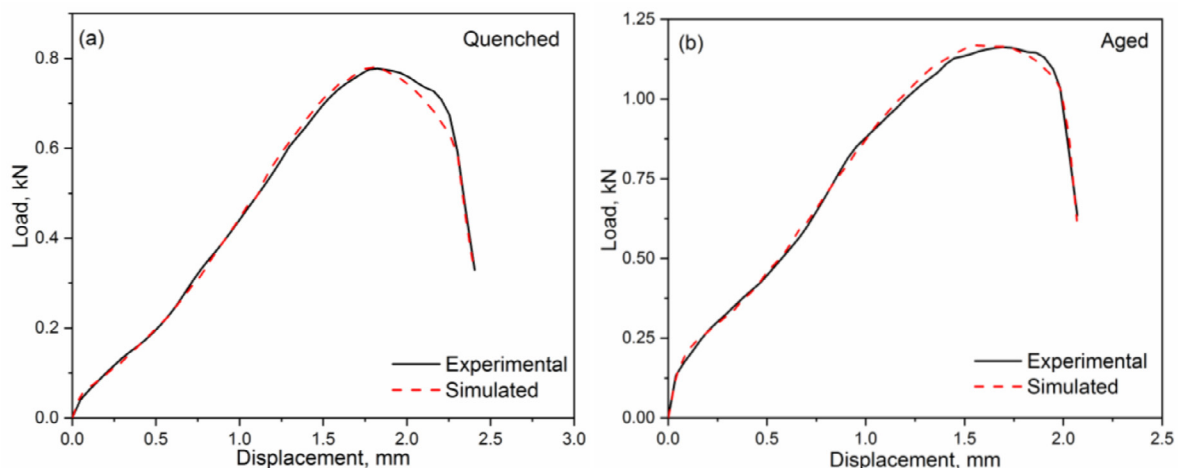

Fig. 8. Experimental and simulated load-displacement curves obtained using optimised GTN parameters and friction coefficient for (a) quenched and (b) aged conditions.
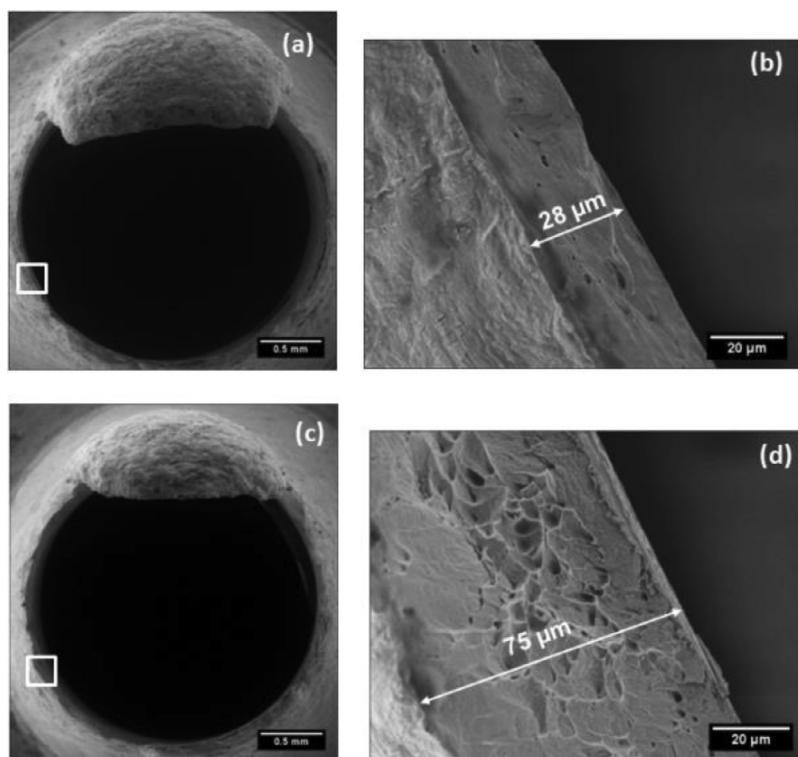
Fig. 9. Location where fractographs were taken for the (a) quenched, (c) aged specimens, (b) and (d) are the corresponding fractographs taken at higher magnifications.
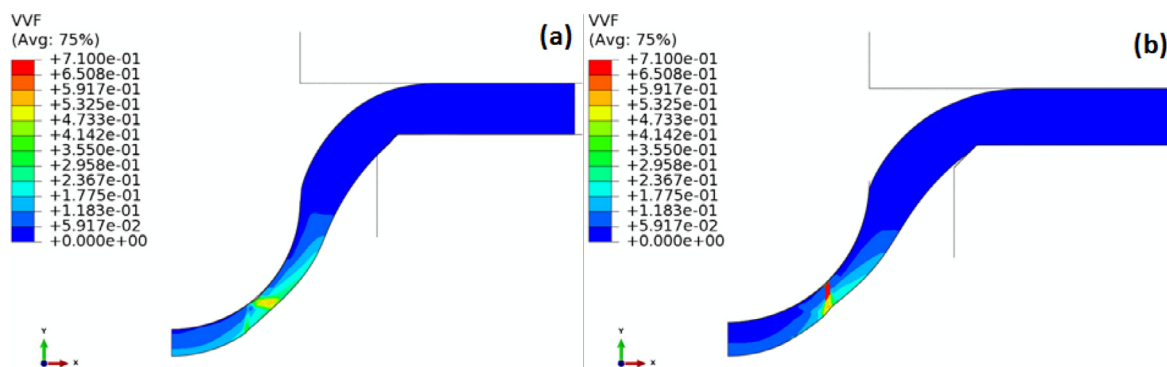

Fig. 10. Distribution of void volume fraction (VVF) at failure for (a) quenched and (b) aged conditions.
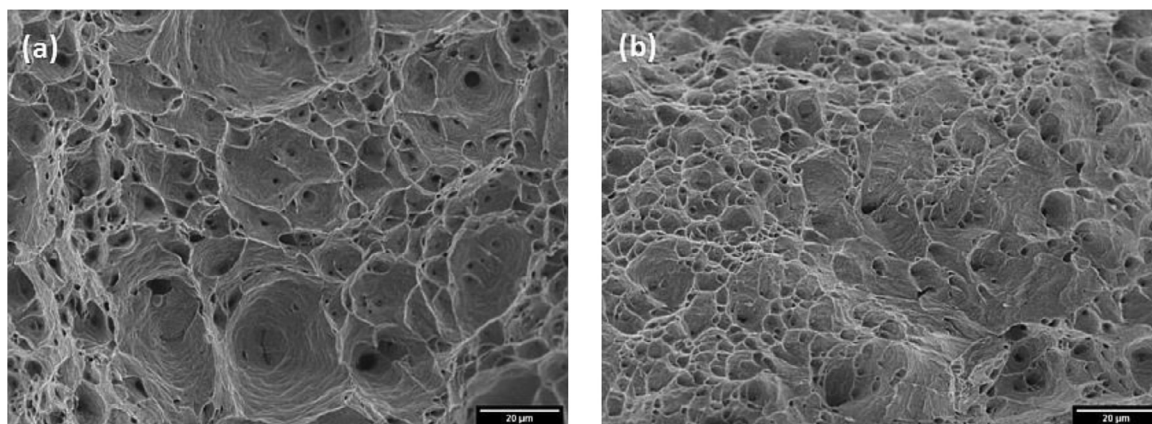

Fig. 11. Fractographs of uniaxially tested (a) quenched and (b) aged specimens.

Final failure in a material occurs due to its lack of load bearing capacity which can be directly related to the reduction in the cross sectional area being tested. The factors which contribute to lowering the load bearing cross section are presence of coalesced voids and localised thinning of the cross section itself. As the material in the quenched condition was relatively ductile, the localized thinning of the cross section contributed significantly to the cross-sectional area reduction. On the other hand the presence of a relatively stronger matrix in the aged condition resisted plastic deformation; therefore the contribution of coalesced voids to the final failure was more dominant when compared to the loss of cross section area due to plastic deformation. This resulted in relatively higher void fraction in case of the aged material at failure.

5. Conclusion

Incorporating elastic and plastic properties in a finite element model could only simulate the initial stages of SPT based load-displacement curves of CuCrZr alloy in both quenched and aged conditions. GTN damage model was used to simulate the complete load-displacement curve for both the conditions. The values of the GTN parameters were determined using an inverse finite element method. Differences in the fractographs of both the conditions could be correlated to the variations in the respective micro-mechanical parameters of the GTN model. A new compliance correction method has been proposed wherein the correction factors can be determined using finite element analysis incorporating only the elastic and plastic properties.

Data availability

The raw/processed data required to reproduce these findings cannot be shared at this time as the data also forms part of an ongoing study.

Declaration of Competing Interest

The authors declare that they have no known competing financial interestsor personal relationships that could have appeared to influence the work reported in this paper.

CRediT authorship contribution statement

V.D. Vijayanand: Writing – original draft, Methodology, Conceptualization, Investigation, Formal analysis, Visualization, Software. **M. Mokhtarishirazabad:** Writing – review & editing, Investigation, Data curation, Validation. **Y. Wang:** Writing – review & editing, Resources, Project administration, Funding acquisition. **M. Gorley:** Writing – review & editing, Resources, Project administration, Funding acquisition. **D.M. Knowles:** Resources, Project administration, Funding acquisition. **M. Mostafavi:** Writing – review & editing, Supervision, Project administration, Funding acquisition.

References

[1] K. Zhang, E. Gaganidze, M. Gorley, Development of the material property handbook and database of CuCrZr, Fusion Eng. Des. 144 (2019) 148–153, doi:10.1016/j.fusengdes.2019.04.094.

[2] J.Y. Park, J.S. Lee, B.K. Choi, B.G. Hong, Y.H. Jeong, Effect of cooling rate on mechanical properties of aged ITER-grade CuCrZr, Fusion Eng. Des. 83 (2008) 1503–1507, doi:10.1016/j.fusengdes.2008.07.006.

[3] U. Holzwarth, H. Stamm, The precipitation behavior of ITER-grade Cu–Cr–Zr alloy after simulating the thermal cycle of hot isostatic pressing, J. Nucl. Mater. 279 (2000) 31–45, doi:10.1016/S0022-3115(99)00285-8.

[4] N. Ordás, L. Portolés, M. Azpeleta, A. Gómez, J.R. Blasco, M. Martinez, J. Ureña, I. Iturriza, Development of CuCrZr via electron beam powder bed fusion (EB-PBF), J. Nucl. Mater. 548 (2021) 152841, doi:10.1016/j.jnucmat.2021.152841.

[5] A.D. Ivanov, A.K. Nikolaev, G.M. Kalinin, M.E. Rodin, Effect of heat treatments on the properties of CuCrZr alloys, J. Nucl. Mater. 307–311 (2002) 673–676, doi:10.1016/S0022-3115(02)01110-8.

[6] V.R. Barabash, G.M. Kalinin, S.A. Fabritsiev, S.J. Zinkle, Specification of CuCrZr alloy properties after various thermo-mechanical treatments and design allowables including neutron irradiation effects, J. Nucl. Mater. 417 (2011) 904–907, doi:10.1016/j.jnucmat.2010.12.158.

[7] Y. Wang, O. Mohamed, K. Dunn, T. Sui, M. Bashir, P. Cooper, A. Lukenskas, G. Wu, M. Gorley, Effects of stress triaxiality and strain rate on the fracture of a CuCrZr alloy, J. Nucl. Mater. 543 (2021) 152546, doi:10.1016/j.jnucmat.2020.152546.

[8] D.J. Edwards, B.N. Singh, S. Tähtinen, Effect of heat treatments on precipitate microstructure and mechanical properties of a CuCrZr alloy, J. Nucl. Mater. 367–370 (2007) 904–909, doi:10.1016/j.jnucmat.2007.03.064.

[9] T.E. García, C. Rodríguez, F.J. Belzunce, C. Suárez, Estimation of the mechanical properties of metallic materials by means of the small punch test, J. Alloys Compd. 582 (2014) 708–717, doi:10.1016/j.jallcom.2013.08.009.

[10] S. Arunkumar, Overview of small punch test, Met. Mater. Int. (2019), doi:10.1007/s12540-019-00454-5.

[11] M. Bruchhausen, S. Holmström, I. Simonovski, T. Austin, J.M. Lapetite, S. Ripplinger, F. de Haan, Recent developments in small punch testing: tensile properties and DBTT, Theor. Appl. Fract. Mech. 86 (2016) 2–10, doi:10.1016/j.tafmec.2016.09.012.

[12] D. Finarelli, M. Roedig, F. Carsughi, Small punch tests on austenitic and martensitic steels irradiated in a spallation environment with 530 MeV protons, J. Nucl. Mater. 328 (2004) 146–150, doi:10.1016/j.jnucmat.2004.04.320.

[13] E. Fleury, J.S. Ha, Small punch tests to estimate the mechanical properties of steels for steam power plant: I. mechanical strength, Int. J. Press. Vessel. Pip. 75 (1998) 699–706, doi:10.1016/S0308-0161(98)00074-X.

[14] C.S. Catherine, J. Messier, C. Poussard, S. Rosinski, J. Foulds, Small punch test: EPRI-CEA finite element simulation benchmark and inverse method for the estimation of elastic plastic behavior, ASTM Spec. Tech. Publ. 1418 (2002) 350–370.

[15] S. Yang, Y. Cao, X. Ling, Y. Qian, Assessment of mechanical properties of incoloy800h by means of small punch test and inverse analysis, J. Alloys Compd. 695 (2017) 2499–2505, doi:10.1016/j.jallcom.2016.11.151.

[16] A. Husain, D.K. Sehgal, R.K. Pandey, An inverse finite element procedure for the determination of constitutive tensile behavior of materials using miniature specimen, Comput. Mater. Sci. 31 (2004) 84–92, doi:10.1016/j.commatsci.2004.01.039.

[17] V.D. Vijayanand, M. Mokhtarishirazabad, J. Peng, Y. Wang, M. Gorley, D.M. Knowles, M. Mostafavi, A novel methodology for estimating tensile properties in a small punch test employing in-situ DIC based deflection mapping, J. Nucl. Mater. 538 (2020) 152260, doi:10.1016/j.jnucmat.2020.152260.

[18] I. Peñuelas, I.I. Cuesta, C. Betegón, C. Rodriguez, F.J. Belzunce, Inverse determination of the elastoplastic and damage parameters on small punch tests, Fatigue Fract. Eng. Mater. Struct. 32 (2009) 872–885, doi:10.1111/j.1460-2695.2009.01387.x.

[19] J.S. Cheon, C.H. Joo, Small punch test for determining a flow stress by using a hybrid inverse procedure, Comput. Mater. Sci. 43 (2008) 744–751, doi:10.1016/j.commatsci.2008.01.052.

[20] M. Eskner, R Sandstrom, Mechanical property evaluation using the small punch test, J. Test. Eval. 32 (2004) 282–289, doi:10.1520/JTE11504.

[21] S. Haroush, E. Priel, D. Moreno, A. Busiba, I. Silverman, A. Turgeman, R. Shneck, Y. Gelbstein, Evaluation of the mechanical properties of SS-316L thin foils by small punch testing and finite element analysis, Mater. Des. 83 (2015) 75–84, doi:10.1016/j.matdes.2015.05.049.

[22] K. Li, J. Peng, C. Zhou, Construction of whole stress-strain curve by small punch test and inverse finite element, Results Phys. 11 (2018) 440–448, doi:10.1016/j.rinp.2018.09.024.

[23] A.L. Gurson, Continuum theory of ductile rupture by void nucleation and growth. Part I. yield criteria and flow rules for porous ductile media, ASME. J. Eng. Mater. Technol. 99 (1) (1977) 2–15, doi:10.1115/1.3443401.

[24] A. Needleman, V. Tvergaard, An analysis of ductile rupture in notched bars, J. Mech. Phys. Solids 32 (1984) 461–490, doi:10.1016/0022-5096(84)90031-0.

[25] A. Lotfolahpour, N. Soltani, M. Ganjiani, D. Baharlouei, Parameters identification and validation of plastic-damage model of 304 stainless steel by small punch test at ambient temperature, Eng. Fract. Mech. 200 (2018) 64–74, doi:10.1016/j.engfracmech.2018.07.007.

[26] I.I. Cuesta, J.M. Alegre, R. Lacalle, Determination of the gurson–tvergaard damage model parameters for simulating small punch tests, Fatigue Fract. Eng. Mater. Struct. 33 (2010) 703–713, doi:10.1111/j.1460-2695.2010.01481.x.

[27] CEN workshop agreement, CWA 15627:2006 E, small punch test method for metallic materials, CEN, Brussels, Belgium, (n.d.).

[28] D. Sánchez-Ávila, A. Orozco-Caballero, E. Martínez, L. Portolés, R. Barea, F. Carreño, High-accuracy compliance correction for nonlinear mechanical testing:

improving small punch test characterization, Nucl. Mater. Energy 26 (2021) 100914, doi:10.1016/j.nme.2021.100914.

[29] E.N. Campitelli, P. Spätig, R. Bonadé, W. Hoffelner, M. Victoria, Assessment of the constitutive properties from small ball punch test: experiment and modeling, J. Nucl. Mater. 335 (2004) 366–378, doi:10.1016/j.jnucmat.2004.07.052.

[30] M. Li, S.J. Zinkle, Physical and mechanical properties of copper and copper alloys, Compr. Nucl. Mater. (2012) 667–690, doi:10.1016/B978-0-08-056033-5.00122-1.

[31] Y. Ruan, P. Spätig, M. Victoria, Assessment of mechanical properties of the martensitic steel-EUROFER97 by means of punch tests, J. Nucl. Mater. 307–311 (2002) 236–239, doi:10.1016/S0022-3115(02)01194-7.

[32] J.C. Chica, P.M. Bravo Díez, M.P Calzada, Improved correlation for elastic modulus prediction of metallic materials in the small punch test, Int. J. Mech. Sci. 134 (2017) 112–122, doi:10.1016/j.ijmecsci.2017.10.006.

[33] M. Abendroth, M. Kuna, Determination of ductile material properties by means of the small punch test and neural networks, Adv. Eng. Mater. 6 (2004) 536–540, doi:10.1002/adem.200400405.

[34] J. Peng, V.D. Vijayanand, D. Knowles, C. Truman, M. Mostafavi, The sensitivity ranking of ductile material mechanical properties, geometrical factors, friction coefficients and damage parameters for small punch test, Int. J. Press. Vessel Pip. (2021) 104468, doi:10.1016/j.ijpvp.2021.104468.

[35] V. Tvergaard, Influence of voids on shear band instabilities under plane strain conditions, Int. J. Fract. 17 (1981) 389–407, doi:10.1007/BF00036191.

[36] S.N. Sivanandam, S.N. Deepa, Genetic algorithms BT, in: S.N. Sivanandam, S.N. Deepa (Eds.), Introduction to Genetic Algorithms, Springer Berlin Heidelberg, Berlin, Heidelberg, 2008, pp. 15–37, doi:10.1007/978-3-540-73190-02.

[37] M. Abendroth, H. Zielke, Numerical investigation of the influence of friction in SPT experiments, Ubiquity Proc. 1 (2018) 1, doi:10.5334/uproc.1.

[38] ASM handbookVolume 12, Fractography, American Society for Metals, Metals Park, Ohio, 1987.

[39] G.E. Dieter, D.J. Bacon, D. Bacon, Mechanical Metallurgy, McGraw-Hill, 1988 https://books.google.co.uk/books?id=hlabmB3e8XwC.

[40] G.L. Roy, J.D. Embury, G. Edwards, M.F. Ashby, A model of ductile fracture based on the nucleation and growth of voids, Acta Metall. 29 (1981) 1509–1522, doi:10.1016/0001-6160(81)90185-1.

[41] C.C. Chu, A. Needleman, Void nucleation effects in biaxially stretched sheets, J. Eng. Mater. Technol. 102 (1980) 249–256, doi:10.1115/1.3224807.

[42] P. Noell, J. Carroll, K. Hattar, B. Clark, B. Boyce, Do voids nucleate at grain boundaries during ductile rupture? Acta Mater. 137 (2017) 103–114, doi:10.1016/j.actamat.2017.07.004.